The Astronomical Journal, 170:127 (11pp), 2025 August https://doi.org/10.3847/1538-3881/adea50

Spectroscopy of Free-floating Planetary-mass Objects and Their Disks with JWST

Belinda Damian[1], Aleks Scholz[1], Ray Jayawardhana[2], V. Almendros-Abad[3], Laura Flagg[2], Koraljka Mužić[4], Antonella Natta[5], Paola Pinilla[6], and Leonardo Testi[7]
[1] SUPA, School of Physics & Astronomy, University of St Andrews, North Haugh, St Andrews KY16 9SS, UK; bd64@st-andrews.ac.uk
[2] Department of Physics & Astronomy, Johns Hopkins University, Baltimore, MD 21218, USA
[3] Istituto Nazionale di Astrofisica (INAF)—Osservatorio Astronomico di Palermo, Piazza del Parlamento 1, 90134, Palermo, Italy
[4] Instituto de Astrofísica e Ciências do Espaço, Faculdade de Ciências, Universidade de Lisboa, Ed. C8, Campo Grande, 1749-016 Lisbon, Portugal
[5] School of Cosmic Physics, Dublin Institute for Advanced Studies, 31 Fitzwilliam Place, Dublin 2, Ireland
[6] Mullard Space Science Laboratory, University College London, Holmbury St Mary, Dorking, Surrey, UK
[7] Dipartimento di Fisica e Astronomia, Università di Bologna, Via Gobetti 93/2, 40122, Bologna, Italy
Received 2025 April 30; revised 2025 June 27; accepted 2025 June 28; published 2025 July 30

Abstract

Free-floating planetary-mass objects (FFPMOs) are known to harbor disks at young ages. Here, we present 1–13 μm spectra for eight young FFPMOs with masses of 5–10 $M_{\rm Jup}$ (at ages of 1–5 Myr), using the NIRSpec and MIRI instruments on the James Webb Space Telescope. We derive fundamental properties of these targets, and find spectral types of M9.5 to L4, with effective temperatures of 1600–1900 K. The photospheric spectra of our targets show a clear diversity at similar temperatures, especially in the 3–5 μm range, unaccounted for by existing atmospheric models. We find a silicate absorption feature in the photosphere of one of our targets, the first such detection in very young FFPMOs, indicating silicate clouds in their cool atmospheres. Six of our objects show mid-infrared excess emission above the photosphere, as well as silicate emission features, demonstrating the presence of disks. The shape and strength of the latter features constitute strong evidence of grain growth and crystallization, similar to what is seen in more massive brown dwarfs and stars. We also detect emission lines from hydrocarbon molecules in the disks of several targets. These are the lowest-mass isolated objects found so far with silicate and hydrocarbon emission features arising in their disks. The presence of disks and their characteristics point to the potential for the formation of rocky companions around free-floating planetary-mass objects.

Unified Astronomy Thesaurus concepts: Free floating planets (549); Protoplanetary disks (1300); Infrared excess (788); James Webb Space Telescope (2291); Infrared spectroscopy (2285)

1. Introduction

In the year 2000, two groups reported discoveries of the first isolated objects with masses below the deuterium-burning limit (P. W. Lucas & P. F. Roche 2000; M. R. Zapatero Osorio et al. 2000). They were found as members of the σ Orionis and the Orion Nebula young clusters, as a low-mass extension of the population of free-floating brown dwarfs. Not being able to ignite any fusion reactions, their masses are in the same realm as those of giant planets, with corresponding spectral types of very late M or early L (at young ages). Since then, samples of such free-floating planetary-mass objects (FFPMOs) have been found in several star-forming regions surveyed with sufficient depth (K. L. Luhman 2007; A. Scholz et al. 2012; N. Miret-Roig et al. 2022; E. L. Martín et al. 2025). Similar objects have also been found in young stellar associations and in the field (P. Delorme et al. 2012; A. C. Schneider et al. 2016).

The existence of FFPMOs raises several important questions about the processes that form stars and planets. For example: (1) What is the lowest mass limit for an object to form like a star?; (2) What physical conditions foster or inhibit the formation of such objects?; (3) How many giant planets are ejected early in their evolution to form a population of rogue planets?; and, finally, (4) Can FFPMOs form their own miniature planetary systems (and should these companions be referred to as planets or moons)? Observationally, addressing these questions requires both the identification of FFPMOs in diverse regions and detailed characterization of their properties. These goals can be accomplished with the aid of the supreme infrared sensitivity of the James Webb Space Telescope (JWST) and its suite of excellent instruments (J. Rigby et al. 2023).

For more than two decades, it has been established that disks are found around brown dwarfs with masses around and below the deuterium-burning limit (A. Natta & L. Testi 2001; R. Jayawardhana et al. 2003; K. L. Luhman et al. 2005; A. Scholz & R. Jayawardhana 2008; B. Damian et al. 2023a). The primary evidence for the presence of disks around FFPMOs came from the excess flux observed in the infrared 3–8 μm bands compared to the photosphere. Further characterization of these FFPMO disks was hampered by the low luminosity of such targets. Prior to JWST, only one FFPMO had a (low signal-to-noise ratio) mid-infrared spectrum (V. Joergens et al. 2013); the same object also has a submillimeter detection (A. Bayo et al. 2017). With the enhanced mid-infrared sensitivity of JWST, we are now in a position to improve upon these earlier detections and to conduct a more comprehensive survey of the FFPMO disks.

We have observed eight planetary-mass objects suspected of hosting disks with JWST, obtaining spectra from 1 to 13 μm. For one of these objects, CHA1107-7626, we have recently published JWST spectra, highlighting the presence of hydrocarbon molecular emission lines in the mid-infrared (L. Flagg et al. 2025). In this paper, we present a full analysis of JWST

Table 1
List of Targets Observed for This Paper, in Order of R.A., with Newly Determined Properties

Object	R.A. (deg)	Decl. (deg)	SpT Lit.	SpT This Work	$T_{\rm eff}$ (K)	A_V Lit. (mag)	A_V This Work (mag)	Distance (pc)	M_J (mag)	Radius ($R_{\rm Jup}$)
UGC0417+2832[a]	64.4916	+28.5426	M9–L7 (L3)	L4	1600	3.67	4.3	126 ± 5	12.91	1.8
UGC0422+2655[a]	65.5057	+26.9201	L1	L2	1700	2.07	2.4	163 ± 3	11.39	2.9
UGC0433+2251[a]	68.4753	+22.8553	L0.5	L2	1600	1.56	1.3	157 ± 9	11.63	2.9
UGC0439+2642[a]	69.7823	+26.7100	M9.5–L4 (L1)	M9.5	1800	2.07	5.6	139 ± 6	11.00	2.5
CHA1107-7626[b]	166.7820	−76.4424	M9–L1 (L0)	M9.5	1800	0.00	1.4	195 ± 4	10.79	2.8
CHA1110-7633[c]	167.6743	−76.5518	M9–L3 (L0)	M9.5	1800	7.52	7.0	193 ± 2	10.12	3.8
CHA1110-7721[c]	167.7085	−77.3649	M9–L2 (L0)	L2	1700	5.37	4.6	190 ± 6	11.09	3.1
UHWJ247.95-24.78[d]	247.9543	−24.7806	L1	L1	1900	0.00	2.6	145 ± 5	11.15	2.2

Notes. The prefix "UGC" indicates targets belonging to the Taurus region, "CHA" for targets in Chamaeleon I, and "UHW" for the target in ρ Ophiuchus. The spectral type (SpT), effective temperature ($T_{\rm eff}$), extinction (A_V), and radius are derived in Section 3. The distance to each target is estimated in Section 2.
References for spectral type and extinction:
[a] T. L. Esplin & K. L. Luhman (2019),
[b] K. L. Luhman et al. (2008),
[c] T. L. Esplin et al. (2017),
[d] K. N. Allers & M. C. Liu (2020).
The spectral types given within the brackets indicate the values adopted in the respective works. The A_J values from literature were transformed to A_V using the K. D. Gordon et al. (2023) relation.

infrared spectra for the entire sample, focused on the empirical characterization. In Section 2, we present the targets, the data set, and the reduction. Section 3 focuses on the analysis of the near-infrared data from 1 to 5 μm. The mid-infrared spectra from 5 to 12 μm are discussed in Section 4. We discuss and summarize the outcomes of our work in Section 5.

2. The JWST Data Set

2.1. Target Selection

The goal of this project was to investigate potential disks around isolated objects with masses significantly below the deuterium-burning limit. For this purpose, we searched the literature for objects that are (a) members of young (1–3 Myr), nearby (<200 pc) star-forming regions, (b) have spectral types of early L, indicating masses of 5–10 $M_{\rm Jup}$ for such young ages, and (c) show signs of infrared excess emission in Spitzer/IRAC (Infrared Array Camera) photometry. We identified eight good candidates, in three star-forming regions—four in Taurus, three in Chamaeleon I, and one in ρ Ophiuchus—listed in Table 1. All eight are among the lowest-mass isolated objects with some evidence for infrared excess, all identified as members of star-forming regions. For all eight, a ground-based near-infrared spectrum and photometry are available in the literature; see Table 1 for references. In this paper we provide a new determination of their fundamental properties using the higher-quality data obtained from JWST.

The distances to our FFPMOs were estimated using Gaia DR3 (Gaia Collaboration et al. 2016, 2023). Our targets are themselves too faint to be detected by Gaia; however, many stellar members of the same star-forming regions have well-determined parallaxes. For each target, we identified around 8–10 young stars in the same star-forming region that are closest to the target, using cluster membership catalogs by T. L. Esplin et al. (2017) for Chamaeleon I, T. L. Esplin & K. L. Luhman (2019) for Taurus, and T. L. Esplin & K. L. Luhman (2020) for ρ Ophiuchus. We adopted the mean distance and the standard deviation of these stellar neighbors derived from the Gaia DR3 parallax values as proxy for the distance and corresponding uncertainty to the given target. These distances are presented in Table 1. The estimated distances from Gaia DR3 are consistent within the uncertainty with the distances measured by C. A. L. Bailer-Jones et al. (2021).

In Figure 1 we compare the infrared colors of our targets with those of young stars, brown dwarfs, and planetary-mass objects. The figure shows an infrared color–magnitude diagram for two star-forming regions, compiled from the literature, with our eight targets overplotted and labeled. The K and 4.5 μm magnitudes for our targets are from K. L. Luhman et al. (2008), T. L. Esplin et al. (2017), and T. L. Esplin & K. L. Luhman (2019, 2020). The magnitudes were transformed to absolute magnitudes using the A_V and distance from Table 1 and the extinction relations of K. D. Gordon et al. (2023; see also E. L. Fitzpatrick 1999; K. D. Gordon et al. 2009, 2021; M. Decleir et al. 2022 used by K. D. Gordon et al. 2023). The figure also includes isochrones from two models for an age of 2 Myr from I. Baraffe et al. (2015) and M. W. Phillips et al. (2020). The plot illustrates that according to their absolute magnitudes these objects have masses below or around 0.01 $M_\odot$. In addition, their $K - 4.5$ μm color is enhanced compared to the photospheric color, likely due to the presence of a surrounding disk.

2.2. Observations and Reduction

All eight targets were observed as part of program 4583[8] in JWST cycle 3 between 2024 August 21 and October 8. We used the prism mode on the Near-Infrared Spectrograph (NIRSpec) and the low-resolution spectroscopy (LRS) mode on the Mid-Infrared Instrument (MIRI) to cover the spectrum from 1 to 13 μm at a low resolution of ~100. The setup was identical for all eight targets.

For NIRSpec, we used the S200A1 slit, the full subarray, and the NRSIRS2RAPID readout mode. With three dithers,

[8] The JWST data presented in this article were obtained from the Mikulski Archive for Space Telescopes (MAST) at the Space Telescope Science Institute. The specific observations analyzed can be accessed via doi: 10.17909/xqx9-v187.

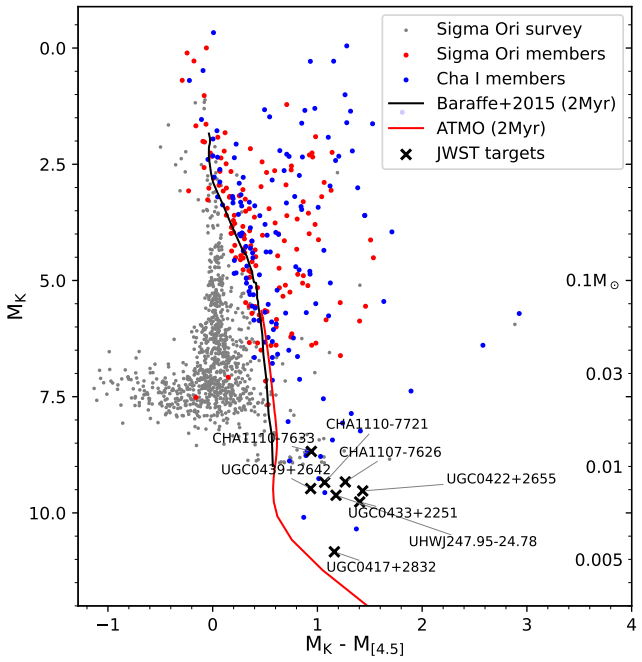

Figure 1. A $K-4.5$ μm color–magnitude diagram highlighting the location of our objects observed with JWST along with the distribution of low-mass members from the σ Orionis (B. Damian et al. 2023b) and Chamaeleon I (T. L. Esplin et al. 2017) star-forming regions of a similar age. The magnitudes are in absolute scale, transformed using their respective extinction and distance to the cluster (see Table 1 for values). The black and red curves show the 2 Myr isochrones from I. Baraffe et al. (2015) and M. W. Phillips et al. (2020), respectively. Masses corresponding to the K-band magnitudes are on the right.

three integrations per exposure, and four groups per integration, the total on-source time was 656.5 s for each target. For MIRI, we used the full subarray, with dithers along the slit, and FASTR1 readout pattern. The total on-source time per target was 3591 s, split into two dithers, eight integrations per exposure, and 80 groups per integration. When designing the program, the goal was to achieve a signal-to-noise ratio above 100 for the 1–3 μm domain, and above 10 up to 13 μm. In total, the program used 22.2 hr of telescope time.

In the following, we use the JWST spectra produced with pipeline version 1.15.1 (H. Bushouse et al. 2024) with the default settings. The CRDS versions and context used by the JWST pipeline were 12.0.9 and jwst_1322.pmap, respectively. We found that the pipeline products are of excellent quality. Apart from cosmetic removal of a couple of outlying data points, we did not introduce any further reduction steps. From the MIRI 5 μm verification images, we see that all our targets appear to be isolated single-source objects. In Figure 2 we show the complete reduced data set for our eight targets, including the NIRSpec (green) and MIRI (orange) spectra, along with the available infrared photometry. The NIRSpec and MIRI spectra match each other well at 5 μm. In general, the photometry also matches the spectra, especially considering that the photometry is over 10 yr old and young objects are expected to show some level of variability. The spectra show minimal noise for most of the wavelength range covered. We note that beyond 11 μm the noise level increases, but we can still make useful flux estimates up to 13 μm.

3. The Photospheric Spectra

In this section we analyze the NIRSpec spectra from 1 to 5 μm, focusing on deriving the photospheric properties of our targets.

3.1. Spectral Type Fitting

We first determine the spectral type and extinction by fitting our spectra (from 1 to 2.5 μm) to a grid of reddened standard templates. Our methodology is similar to that used by B. Damian et al. (2023b) and A. B. Langeveld et al. (2024). The set of standard spectral templates we have used are as follows:

1. M0–L0 (at intervals of 0.5 subclass), L2, L4, and L7 templates from K. L. Luhman et al. (2017).
2. L1 and L6 from K. N. Allers & M. C. Liu (2013) for objects 2MASS J05184616-2756457 and 2MASS J22443167+2043433 respectively.
3. L3 from K. N. Allers & M. C. Liu (2013) constructed as an average of three objects proposed by K. L. Cruz et al. (2018).
4. L5 proposed by L. Piscarreta et al. (2024) for 2MASS J21543454-1055308, with the spectrum obtained from J. Gagné et al. (2015).
5. M4–L9 (for every 1 subclass) old field dwarfs from the SpeX prism spectral library (A. J. Burgasser 2014).

To indicate the age of the templates, we use the prefix "Y" for young and "F" for old field dwarfs. All the templates listed above with numbers 1, 2, 3, and 4 are considered as young dwarfs ("Y"): M0–L0, L2, L4, and L7 have ages <5 Myr; L1, L3, L5, and L6 have ages of ~10–100 Myr (refer to K. N. Allers & M. C. Liu 2013; L. Piscarreta et al. 2024 for details) and those under number 5 are considered as old dwarfs ("F").

We calculate the χ^2 goodness of fit of our object spectra with the grid of templates reddened by an A_V between 0 and 10 mag in steps of 0.1 mag using the E. L. Fitzpatrick (1999) extinction law. The choice of extinction law does not have any significant effect on the result, as reported by V. Almendros-Abad et al. (2022). In Figure 3 we show the results for one example—the fitting produces a very good match for a relatively narrow range of spectral type and extinction. The best-fitting spectral type and A_V are reported in Table 1. We visually examine the parameter range close to the best-fit templates by comparing with our spectra. In Figure 3 we show as an example the spectrum of CHA1110-7633 compared with the best fit, and also shifted in subtype by ±0.5 and in A_V by ±1 mag. From this comparison, we infer typical uncertainties of 0.5 subtype and 1 mag in A_V.

We find that all our targets fit well with young templates for spectral types of M9.5 to L4, as expected for planetary-mass members in star-forming regions. For four of our targets our estimates are 1–2 spectral types later than previously reported in the literature (see Table 1), and for three targets they are 0.5–1.5 subtypes earlier. We observe that all our targets have a prominent triangular-shaped peak in the H band that is characteristic of young late M-type and cooler objects (e.g., R. Jayawardhana & V. D. Ivanov 2006; A. Scholz et al. 2012). The extinction A_V ranges from 1.3 to 7 mag. The A_V values estimated above are consistent for most targets with values previously reported in the literature, with differences <0.5–1.5 mag (see Table 1). The two exceptions are

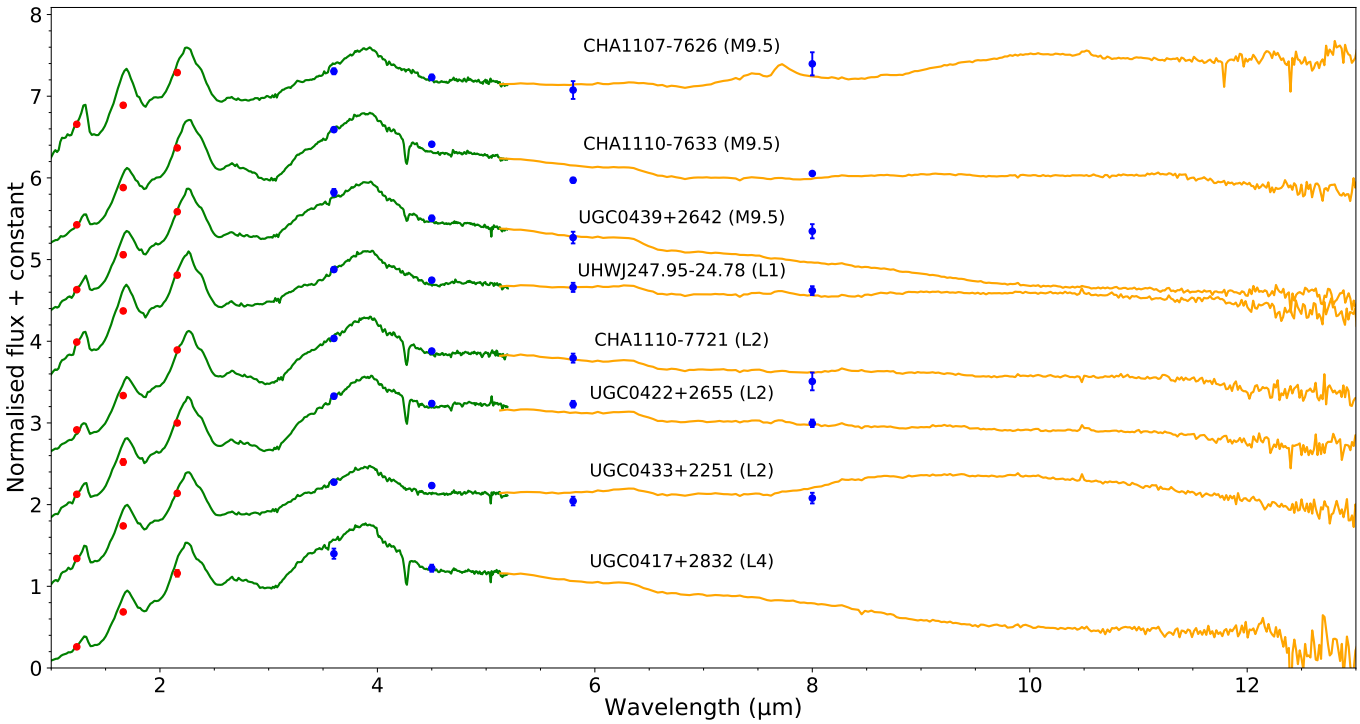

Figure 2. Observed spectra of all the eight objects with JWST NIRSpec (green) and MIRI (orange) normalized to the flux at 2.5 μm. Published photometry at near-infrared (red) and mid-infrared (blue) wavelengths is overplotted.

UGC0439+2642 and UHWJ247.95-24.78, for which our values are ∼2.5–3.5 mag higher than previous estimates by T. L. Esplin & K. L. Luhman (2019) and K. N. Allers & M. C. Liu (2020), respectively.

3.2. Comparison with Model Spectra

We fit the NIRSpec data from 1 to 2.5 μm with the BT-Settl photospheric models (F. Allard et al. 2012). We exclude the 2.5–5 μm range to avoid possible contamination from excess flux due to disk emission. The free parameters in this process are the effective temperature, log g, extinction, and the radius in the dilution factor (R^2/D^2, where R is the radius and D is the distance). We vary the radius between 0.5 and 4 $R_{\rm Jup}$ and A_V between 0.5 mag above and below the value derived from the spectral type fitting. We assume the distances as listed in Table 1. The reduced χ^2 is estimated using the following relation:

$$\chi^2 = \frac{1}{N-4}\sum_{i=1}^{N}\frac{(O_i - E_i)^2}{\sigma_i^2} \quad (1)$$

where N is the number of data points, O is the observed target flux, E is the model flux, and σ is the uncertainty in the observed flux. We use the recent extinction relation from K. D. Gordon et al. (2023) to redden the model spectra. In Figure 4 we present the results for one of our targets (UHWJ247.95-24.78).

For most objects, the BT-Settl models give an acceptable fit to the *JHK* bands. Again, the resulting best-fit effective temperatures and radii are listed in Table 1. The complete spectra (1–13 μm) of all our targets along with their respective photospheric best-fit models are shown in Figure 5. Given that the model spectra are only available in steps of 100 K, the typical uncertainty in $T_{\rm eff}$ will be at least 100 K. We find all our targets to match best with a log g of 3.5, consistent with the expected value for young low-mass objects. We note that some of our $T_{\rm eff}$ estimates tend to be slightly lower than published conversions between spectral type and temperature. For brown dwarfs in young moving groups with spectral types M9.5 to L4, we would expect temperatures of 1600–2100 K (A. Sanghi et al. 2023). These objects would be slightly older than our targets. For very young star-forming regions, the conversion between spectral type and temperature is poorly constrained; at late M spectral type we would expect temperatures below 2500 K (K. Mužić et al. 2014).

We emphasize that the derived temperatures are model-dependent (as effective temperatures always are), and should only be used in conjunction with the given model. A. Sanghi et al. (2023) and S. A. Hurt et al. (2024) observed that the BT-Settl atmospheric models produce lower temperatures in some dwarfs in the M–L transition region when compared to temperatures derived from evolutionary models. This results in a pileup of objects at ∼1800 K, creating gaps in the spectral type versus temperature relation at around ∼2000 K. Therefore, using a different wavelength regime or a different model family to compare the spectra would likely yield minor differences in the results.

In Figure 6 we show a Hertzsprung–Russell (H-R) diagram comparing our objects with evolutionary tracks for 0.005 and 0.01 $M_\odot$ for ages of 1–5 Myr. We use the ATMO 2020 CEQ models for the Two Micron All Sky Survey (2MASS) filter system from M. W. Phillips et al. (2020). For this purpose we calculate absolute J-band magnitude from the available photometry, using the distance as derived above and the extinction derived from spectral typing, converted to the J band using the extinction law from K. D. Gordon et al. (2023). For six out of the eight targets, the position in the H-R diagram is consistent with the evolutionary track for 0.005 $M_\odot$, for ages of 1–2 Myr. The exceptions are UGC0417+2832, which is

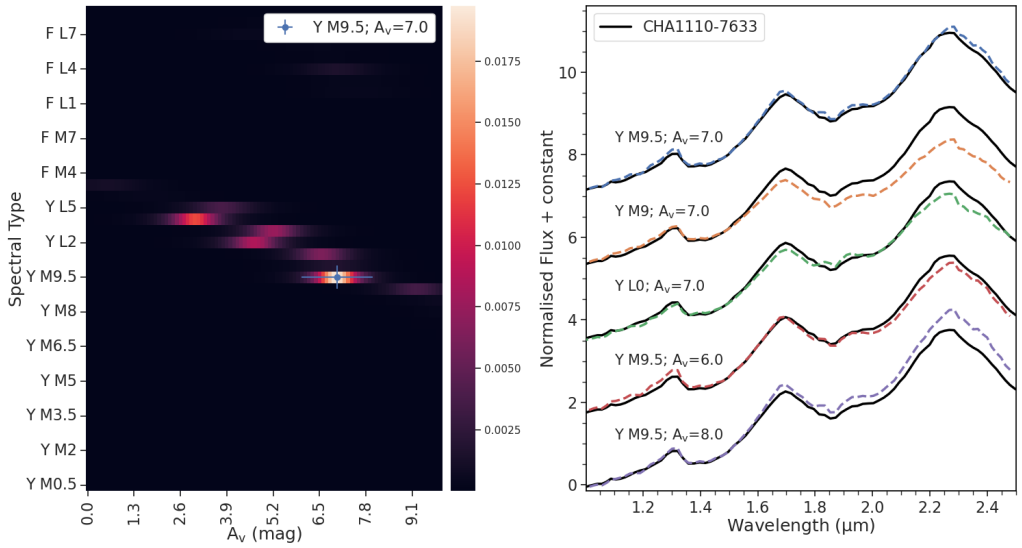

Figure 3. Left: map of A_V vs. spectral type of one of our targets (CHA1110-7633). The order of templates on the y-axis has no significance and they are only grouped according to their ages. The spectral types prefixed with "Y" and "F" indicate the young dwarfs and old field dwarfs, respectively. The color bar indicates the normalized $1/(\chi^2)^2$ value where the lowest χ^2 corresponds to the brightest color. The blue colored marker denotes the best-fitting spectral type and A_V with an uncertainty of 0.5 spectral subtype and 1 mag in extinction (see text for details). Right: NIRSpec spectra of the same object normalized to the flux at 1.5 μm overplotted with the best-fit template and extinction (blue) resampled to match the target resolution. The templates with $\pm$0.5 subtype and $\pm$1 mag in extinction are shown in different colors for comparison.

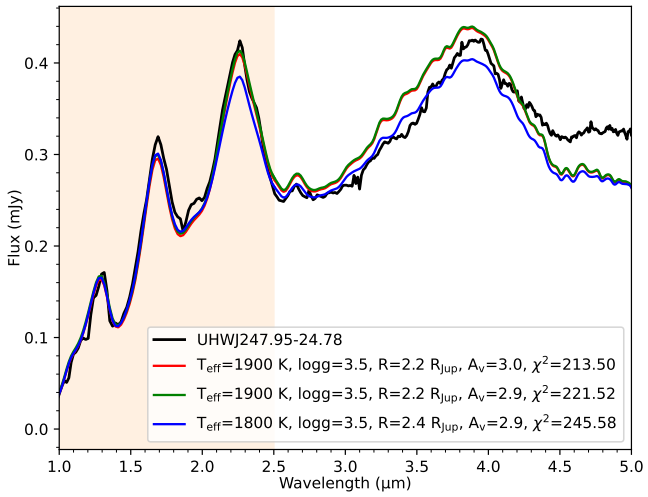

Figure 4. NIRSpec spectrum of UHWJ247.95-24.78 overplotted with the three best-fitting photospheric models reddened and scaled by the corresponding A_V and radius as indicated. The wavelength range considered for the comparison is highlighted by the shaded region. We find that the object fits best with the model spectra for an effective temperature of 1900 K and A_V of 3 mag.

underluminous, and CHA1110-7633, which is overluminous compared to this model, but still too cool for the model at higher mass. Notably, CHA1110-7633 is the source with the highest A_V in the sample. Based on the H-R diagram, all our objects should have masses conservatively below 0.01 $M_\odot$, for the plausible age range adopted here. We note that this conclusion is robust against minor changes in the model-dependent effective temperatures.

3.3. Discussion: Photospheric Spectra of Young Planetary-mass Objects

In Figure 7 we show the 1–5 μm spectra of two of our targets, CHA1107-7626 (M9.5) and UGC0417+2832 (L4), whose spectral types are representative of the range observed in our sample. We compare their spectra with those of two well-studied objects with similar spectral types, TWA 28 and VHS 1256 b. TWA 28 (SSSPMJ1102-3431; R. D. Scholz et al. 2005) is a well-studied brown dwarf member of the TW Hydrae association (age $\sim$10 Myr) with an effective temperature of $\sim$2600 K (M9) and mass around 20 $M_{\rm Jup}$ (L. Venuti et al. 2019; E. Manjavacas et al. 2024). E. Manjavacas et al. (2024) observed this object with JWST NIRSpec in medium resolution ($R \sim 2700$). B. E. Miles et al. (2023) carried out similar medium-resolution observations with the same instrument for VHS 1256 b, a planetary-mass companion to an M dwarf binary system at a distance of $\sim$20 pc (T. J. Dupuy et al. 2020) aged $\sim$140 Myr (T. J. Dupuy et al. 2023) with temperature $\sim$1200 K (L7) and mass $<$20 $M_{\rm Jup}$ (B. E. Miles et al. 2023).

As illustrated in the figure, objects with spectral type from mid-M and beyond show water absorption features in the near- and mid-infrared regimes due to the presence of water vapor in their atmospheres. The depth of these features changes with decreasing temperature (K. N. Allers & M. C. Liu 2013). In Figure 7 we see strong water absorption features at 1.3–1.6 μm, 1.69–2.05 μm, and 2.5–3 μm in all four spectra. We also see prominent CO absorption around 2.4 μm and 4.4–5 μm in VHS 1256 b, but it is weaker in the other three objects. The CO_2 molecular absorption feature at 4.2 μm has been reported only in a few late L and T dwarfs and exoplanets, and is attributed to high metallicity relative to the Sun (T. Tsuji et al. 2011; S. Sorahana & I. Yamamura 2012; JWST Transiting Exoplanet Community Early Release Science Team et al. 2023). Most of our sources, but not all, show a clear absorption dip at this wavelength, of varying strength, something not seen in the models. Accounting for these features requires a more detailed atmospheric analysis beyond the scope of this paper.

In the 3–5 μm spectral domain, the photospheric emission is dominated by a peak that is shaped by water and carbon monoxide

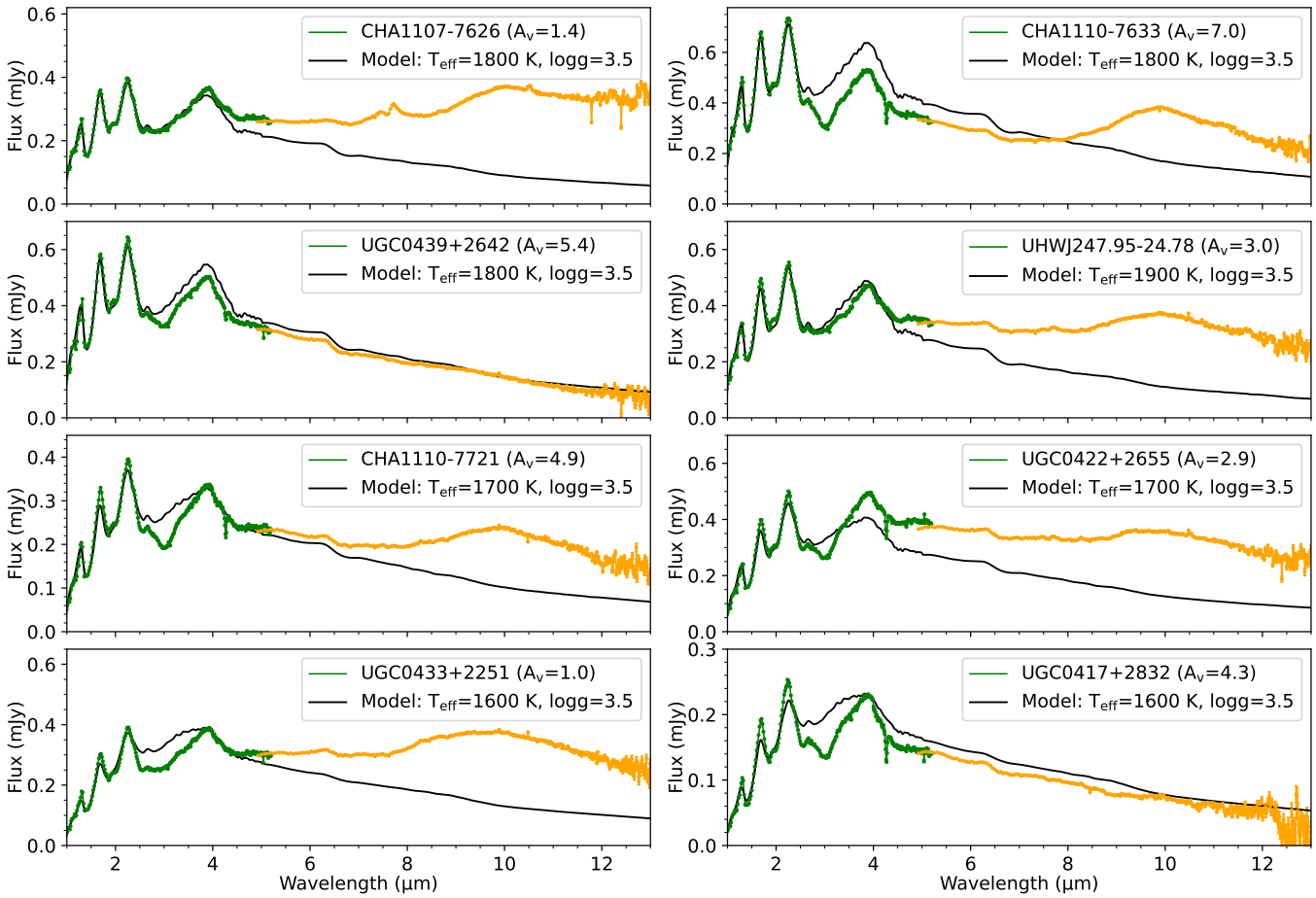

Figure 5. Complete NIRSpec and MIRI spectra of all eight targets dereddened by the extinction estimated through the model fitting along with the best-fit photospheric model from BT-Settl (F. Allard et al. 2012) scaled by the corresponding dilution factor (see text for details).

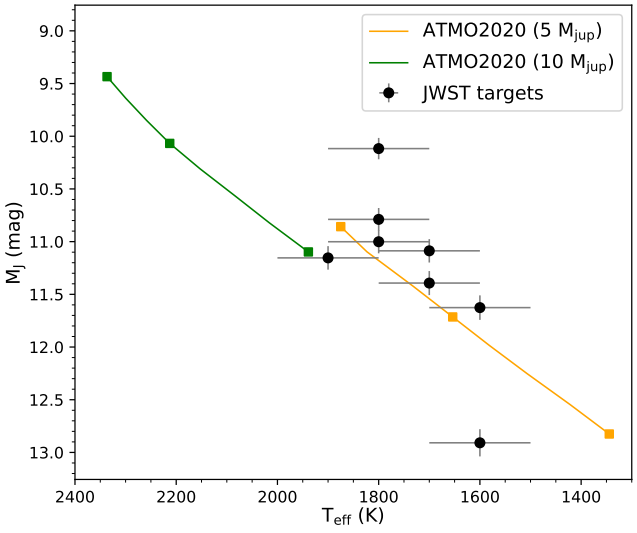

Figure 6. H-R diagram for our sample, in comparison with theoretical evolutionary tracks. The figure shows absolute *J*-band magnitude vs. effective temperature, both listed in Table 1. We overplot error bars assuming errors of ±100 K in temperature and ±10% in brightness. The evolutionary tracks are from ATMO 2020 models (M. W. Phillips et al. 2020) for 0.005 and 0.01 $M_\odot$. The squares on the tracks mark ages of 1, 2, and 5 Myr, from top to bottom.

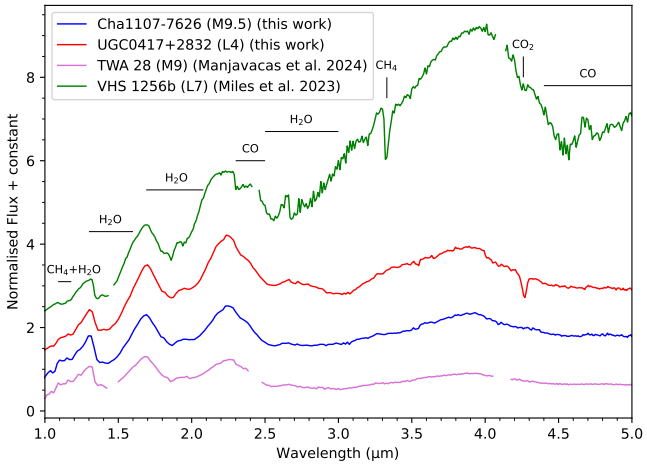

Figure 7. Comparison of spectra of two of our targets with spectra from objects of similar spectral type in the literature. The prominent molecular absorption features are highlighted. The spectra of the literature objects are resampled to match the resolution of our targets and are normalized to the flux at 1.5 μm.

absorption (E. Manjavacas et al. 2024). As seen in Figure 7, the strength of this peak is obviously a function of temperature. As shown in Figures 4 and 5, the 3–5 μm range is often poorly matched by the photospheric models. One object in our sample (UGC0422+2655) shows definitive excess in this band, likely caused by disk emission (see Section 4). Several others have flux levels below those predicted by the model that matches the spectrum in the 1–3 μm range. Clearly, the shape of this feature in the 3–5 μm domain is not properly represented by the models.

As can be appreciated in Figures 2 and 5, the slope between 3 and 3.9 μm is also slightly different when comparing objects in our sample. In about half of the sample, the flux in this range appears to rise with a constant slope (see for example CHA1107-7626 or UGC0433+2251). Some other objects show a minor "bump" at roughly 3.3 μm where the slope flattens (see for example UGC0417+2832 and CHA1110-7721). An example of each type is shown in Figure 7. The presence or absence of this change in 3.3 μm slope is not related to a specific spectral type or the presence of disk emission visible at longer wavelengths. It may be related to extinction—the objects that do not show this tentative bump tend to have low extinction. We note that there is a known methane absorption feature around the same wavelength, visible, for example, in VHS 1256 b (Figure 7). However, our targets are thought to be too warm for methane absorption. There is also known polycyclic aromatic hydrocarbon emission in this wavelength domain; thus, imperfect background subtraction could play a role in affecting the slope of the spectra (C. Boersma et al. 2023). Recently K. L. Luhman & C. Alves de Oliveira (2025) observed the presence of a hydrocarbon absorption feature at 3.4 μm in some very young FFPMOs that otherwise appear to be L dwarfs; we do not see such a feature in any of our sources.

The diversity in the photospheric spectra displayed in our sample points to parameters other than temperature and gravity that influence the spectral appearance in this age and mass range. Apart from variations in metallicity as discussed above, another possibility is inhomogeneity in the cloud distribution (e.g., J. Radigan et al. 2014). In particular, we point to the recent works that show variation in near- and mid-infrared colors and also dust cloud opacity depending on the inclination of the rotational axis relative to the line of sight. The dwarfs with higher inclination angles (equator-on) appear cloudier with redder infrared colors than those with lower inclination angles (pole-on), which appear bluer with lower cloud opacity (J. M. Vos et al. 2017; G. Suárez et al. 2023). Clearly, more work is needed to understand the diversity of cool substellar atmospheres.

4. The Mid-infrared Spectra

In this section we focus on the analysis of the mid-infrared spectra obtained with MIRI/LRS. As discussed in Section 2, our targets were selected based on indications of infrared excess in the available Spitzer photometry. Our comparison with photospheric spectra shows that indeed six out of eight definitively show excess emission beyond 4 μm (Section 3 and Figure 5), as discussed below. For the remaining two sources the mid-infrared spectrum is photospheric; they are further investigated in Section 4.3.

4.1. Mid-infrared Excess from Disks

Six objects in our sample show clear excess emission in the mid-infrared above the photosphere, best appreciated in Figure 5. The additional emission is comparable to or stronger than the photospheric flux around 10 μm. The best explanation for this excess is emission from warm dust in disks. The presence of silicate in emission, typically found in disks around young stars, is also evident in these sources, and will be further analyzed in Section 4.2. Thus, our spectra unambiguously demonstrate the presence of "circum-substellar" material around free-floating planetary-mass objects.

Within this sample there is considerable diversity in the shape of the mid-infrared spectra. Apart from the strength and shape of the silicate feature, the slope of the emission also changes from object to object. In order to measure this, we estimate the extinction-corrected flux ratio at 8.0 μm/3.6 μm. This ratio varies from 0.5 (for Cha1110-7633) to 0.9 (for UGC0433+2251). We note that OTS44, a previously studied planetary-mass object with a disk (V. Joergens et al. 2013), has a slightly larger flux ratio of 0.95 (calculated from photometry).

The slope of the mid-infrared spectral energy distribution (SED) reflects the degree of flaring of the disk and is a proxy for the evolutionary stage of the disk (L. Cieza et al. 2007). Previous work distinguishes between full disks, transitional disks, and evolved disks based on this metric (P. S. Teixeira et al. 2012). This sequence is thought to be linked to the dust evolution—with ongoing grain growth, the dust decouples from the gas and settles to the disk midplane, leading to a lower level of excess emission (e.g., S. Mohanty et al. 2004; A. Scholz et al. 2007).

Our objects show the typical signature of evolved disks, with flat or declining fluxes in the 3–8 μm domain. Beyond 10 μm the flux level also declines in all our objects with disks, with the possible exception of Cha1107-7626. Thus, the slope of the SED provides a first indication of a degree of dust settling and grain growth in disks around planetary-mass objects, as is observed in their more massive counterparts (A. Scholz et al. 2007).

As a side note: With the relatively weak excess emission at 3–8 μm, combined with the low photospheric fluxes, it is challenging to reliably distinguish between objects with and without disks from photometry alone. This is illustrated by the fact that two of the objects in our sample show signs of infrared excess in Spitzer/IRAC photometry, and yet clearly do not harbor disks.

4.2. Silicate Emission Feature in the Disk

In this subsection we parameterize and quantify the shape and strength of the 10 μm silicate emission feature in our targets with disks. This feature is a way to assess the evolutionary state of the warm dust in the inner disk, as has been demonstrated with ground-based (S. Mohanty et al. 2004) and Spitzer data for a number of brown dwarfs (D. Apai et al. 2005; A. Scholz et al. 2007; I. Pascucci et al. 2009). We note that if these objects hold silicate clouds in their cool atmospheres, unlike their higher-temperature and -mass siblings, this would alter the strength of the observed silicate emission feature emanating from the disk (see Section 4.3).

Interstellar extinction can be a contributing factor to undermining the strength and shape of the silicate emission feature arising from the disk, as shown recently by A. M. Arabhavi et al. (2025). Hence, for the following analysis we use the extinction-corrected spectra of our targets. We deredden the spectra using the K. D. Gordon et al. (2023) extinction law and the A_V values derived in Section 3 (see Table 1). The choice of the extinction law stems from its availability in the mid-infrared wavelengths and also because the K. D. Gordon et al. (2023) extinction curve presents the 10 μm feature due to the silicate dust grains in the interstellar medium (ISM). We note that the extinction law does not represent the specific line-of-sight extinction to the targets, and the published extinction

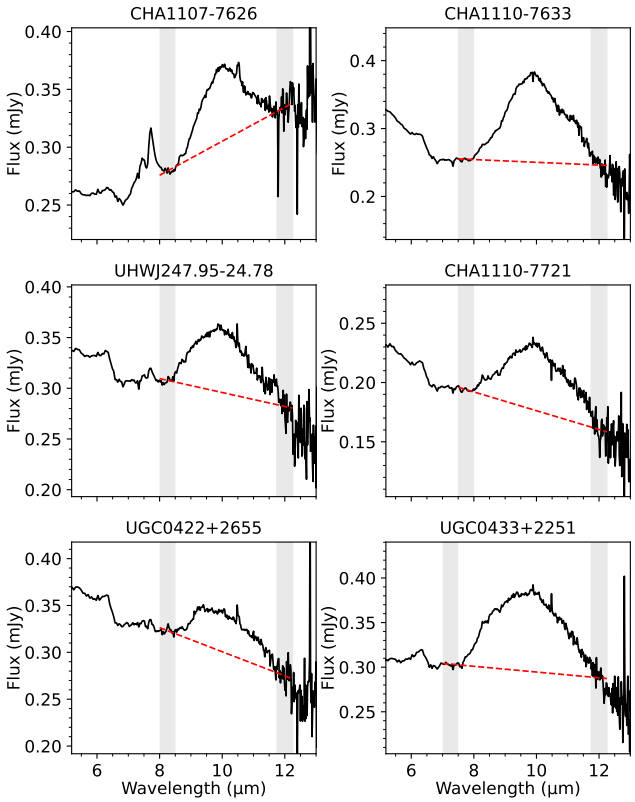

Figure 8. MIRI spectra of our six targets with a disk presented individually in each panel dereddened using the A_V values listed in Table 1. The linear fit to the continuum is shown as a red dashed line and the 0.5 μm wavelength windows used for the fit are shaded in gray. In the shorter wavelength range this was optimized to avoid any emission lines and/or the silicate feature.

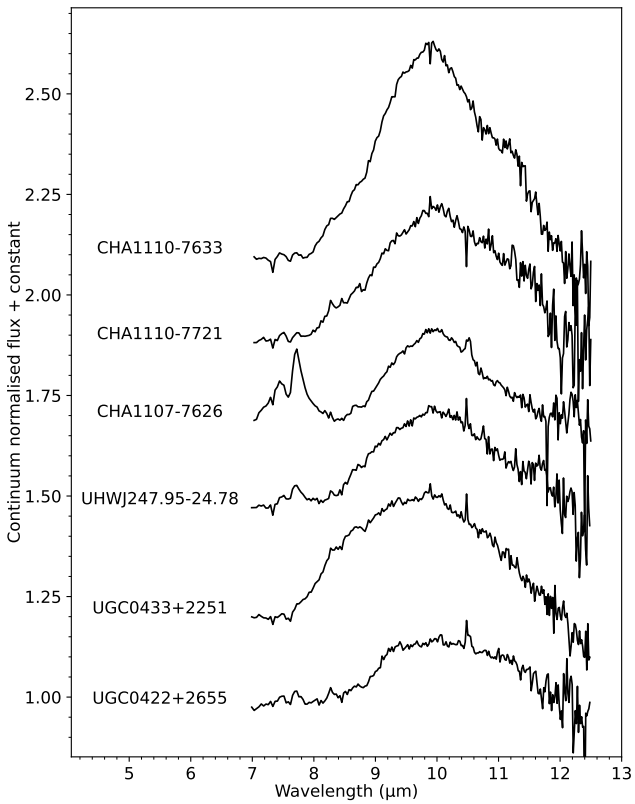

Figure 9. MIRI dereddened spectra normalized to the continuum estimated in the previous figure. We show only the 7–12.5 μm region to highlight the silicate emission feature and the diversity in its shape among our six objects with a disk.

curves are the averages. Hence the differences in the extinction laws may alter the shape of the silicate feature.

To quantify the strength of the silicate feature observed at 10 μm, we first trace a linear fit to the continuum around the feature as shown in Figure 8. We use a wavelength window of 0.5 μm optimized to each object at the bluer end to exclude any emission lines and/or the shoulder of the silicate feature and around 12 μm at the redder end. The wavelength range used to fit the continuum is highlighted in the figure. All six of our targets with disks show an emission feature above the parameterized continuum. We then normalize the spectra to the continuum and estimate the peak flux over the continuum around 10 μm. The prominent emission lines between 9 and 11.5 μm were masked and the spectra was smoothed to obtain the peak flux above the normalized continuum.

The continuum-normalized extinction-corrected spectra are presented in Figure 9, in order of strength of the silicate feature. The plot clearly highlights the diversity in the shape and strength of this feature among our targets, analogous to previous studies for higher-mass brown dwarfs (D. Apai et al. 2005). The variations seen in this figure can be explained by the differences in grain sizes and degree of crystallization. Amorphous ISM-type silicates cause a strong silicate feature, with a single peak around 9–10 μm, as seen in the three objects at the top of Figure 9. On the other hand, crystalline-rich silicates typically show two peaks at 9.3 μm (enstatite) and 11.3 μm (forsterite), resulting in a flattened appearance of the feature, as seen in UGC0422+2655 at the bottom of the plot. For the remaining two objects, the 10 μm feature tends to show a transition state between the amorphous submicron-sized silicate grains and the processed crystalline silicates.

In Figure 10 we plot the continuum-normalized flux ratio at 11.3 versus 9.8 μm and the peak flux over the continuum for the silicate features. For comparison, we also plot the data for the sample of brown dwarfs, T Tauri stars, and Herbig Ae/Be stars from I. Pascucci et al. (2009). This comparison sample from I. Pascucci et al. (2009) is likely derived from spectra that are uncorrected for extinction. Hence, we have shown the distribution of our six FFPMOs both before and after extinction correction. The error bars in the figure indicate the uncertainty in the A_V values and do not represent the possible variations due to the extinction laws.

Prior to extinction correction, our six data points cover the same parameter range as the previously published brown dwarfs, with low values of peak over continuum and flat features (i.e., a flux ratio at 11.3 versus 9.8 μm around 1.0). Dereddening changes primarily the "color" of the silicate feature. It shifts the data points in the figure downwards. Hence, after extinction correction, our data points appear toward the left and below the trend established from the literature.

Overall, the silicate features for some objects in our sample show clear evidence for grain growth and crystallization in disks around planetary-mass objects, similar to what has been observed in higher-mass brown dwarfs. We note that processes that dominate the dust growth such as radial drift are expected to be more efficient around very low-mass objects than around brown dwarfs (P. Pinilla 2022). Combined with the evidence for long-lived dusty disks around planetary-mass objects

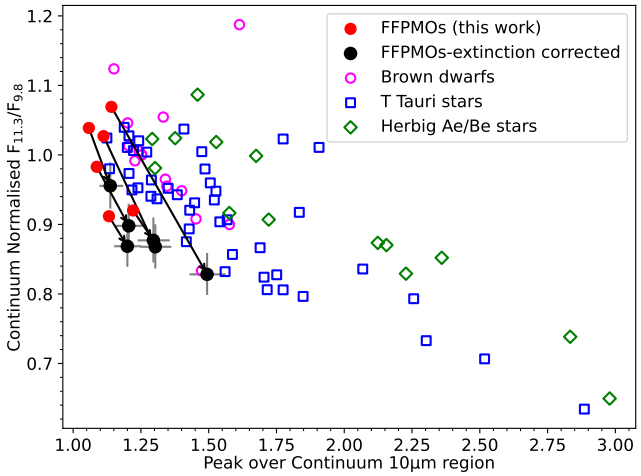

Figure 10. Shape and strength of the silicate emission feature of our FFPMOs with a disk (before and after dereddening) and a sample of brown dwarfs, T Tauri stars, and Herbig Ae/Be stars from I. Pascucci et al. (2009). The error bars indicate the upper and lower values for a change in A_V of ±1 mag. In comparison, this shows that the silicates in the disk around FFPMOs are processed to a higher degree than their massive counterparts.

(A. Scholz et al. 2023; H. H. Seo & A. Scholz 2025), these findings point strongly to the potential for the formation of rocky companions in the disks around free-floating planetary-mass objects.

4.3. Silicate Absorption in the Photosphere

In field brown dwarfs without disks, a silicate absorption feature at 10 μm has been observed, attributed to the presence of silicate clouds in the cool atmospheres (M. C. Cushing et al. 2006; G. Suárez & S. Metchev 2022; and references therein). Besides brown dwarfs, B. E. Miles et al. (2023) recently observed the silicate absorption feature in the MIRI spectra of the planetary-mass companion VHS 1256 b.

For two of our targets, UGC0439+2642 and UGC0417 +2832, which lack excess disk emission in the MIRI spectra above the photospheric models (see Figure 5), we look for evidence of silicate absorption, following a procedure similar to G. Suárez & S. Metchev (2022). We deredden the spectra of these two targets and quantify the silicate index, which is the ratio of the continuum flux to the absorption flux at 9.0 μm. The continuum at 9.0 μm is defined by the best linear fit to the fluxes in a wavelength window of 0.6 μm centered at 7.5 and 11.5 μm as shown in the left panel of Figure 11. We derive the silicate index by estimating the ratio between the average continuum flux and the average absorption flux in a wavelength window of 0.6 μm centered at 9.0 μm. We then compare our results with the silicate index measured for brown dwarfs by G. Suárez & S. Metchev (2022) as a function of their spectral types in the right panel of Figure 11.

We find that one of these two objects, UGC0417+2832, shows silicate in absorption. To our knowledge, this is the first time that silicate absorption has been found in an FFPMO in a young star-forming region (age <10 Myr). The spectrum of the remaining source, UGC0439+2642, is slightly above the photosphere. For both objects, the silicate indices are lower than the median index values of the brown dwarfs for a given spectral type. A larger sample will be required to evaluate how the strength of the silicate absorption changes as a function of spectral type at these very young ages.

4.4. Molecular Gas Lines

Most of the sources analyzed here show mid-infrared emission features attributed to molecular gas in their disks. These features are most pronounced in CHA1107-7626. L. Flagg et al. (2025) reported strong methane (7.7 μm) and ethylene (10.5 μm) emission for this particular object, and discussed similarities in its spectrum with that of a classical T Tauri star, ISO-ChaI 147, observed with JWST/MIRI (A. M. Arabhavi et al. 2024). The detection of hydrocarbon emission features in a planetary-mass object resembling a carbon-rich disk of a low-mass star indicates the similarities in the inner disk conditions across a range of stellar/substellar masses (see also the recent work by A. M. Arabhavi et al. 2025).

While the emission line spectrum for CHA1107-7626 is remarkable, it is by no means unique, as can be appreciated from Figure 9. The 10.5 μm ethylene feature is confidently detected in three other disks in our sample: UGC0422+2655, UHWJ247.95-24.78, and UGC0433+2251. We note that there is also a hydrogen 12–8 line at 10.5 μm that occurs in disks. With the low resolution at this wavelength (of about 0.1 μm), we are unable to decisively distinguish between hydrogen and ethylene. However, none of our spectra show any evidence of other atomic hydrogen lines (R. Franceschi et al. 2024), which should be present in addition to the 12–8 feature. Therefore we deem it more plausible that the observed 10.5 μm emission is due to ethylene.

Similarly, the 7.7 μm methane feature appears to be present in CHA1110-7633, UGC0422+2655, UHWJ247.95-24.78, and CHA1110−7721. Other features may be hidden by the low resolution of our MIRI spectra and/or by the excessive noise beyond 12 μm. Follow-up studies with higher resolution are required to compile a detailed inventory of the molecular line emission in disks around planetary-mass objects.

5. Summary

We present low-resolution 1–13 μm spectra of eight free-floating planetary-mass objects in nearby young star-forming regions observed with the JWST NIRSpec and MIRI instruments. These FFPMOs are members of the young (age <5 Myr) regions Taurus, Chamaeleon I, and ρ Ophiuchus and have masses of 5–10 $M_{\rm Jup}$. All our targets have been previously observed with ground-based spectroscopy and photometry, with indications of infrared excess emission from disks. With our high-quality JWST spectra, we derive fundamental properties of all eight targets and substantiate the presence of disks around six. For the first time in these young planetary-mass objects, we also report the detection of silicate emission in the six objects with disks and a photospheric silicate absorption feature in one of them without a disk.

Our main findings are summarized as follows.

1. By comparing our near-infrared spectra with standard templates, we find the spectral types of our targets to be between M9.5 and L4 with extinction A_V ranging from 1.3 to 7 mag. All our targets produce best-fitting results with young templates, and for most objects the results are consistent with the literature.
2. We also compare our NIRSpec spectra with photospheric models and derive effective temperatures between 1600

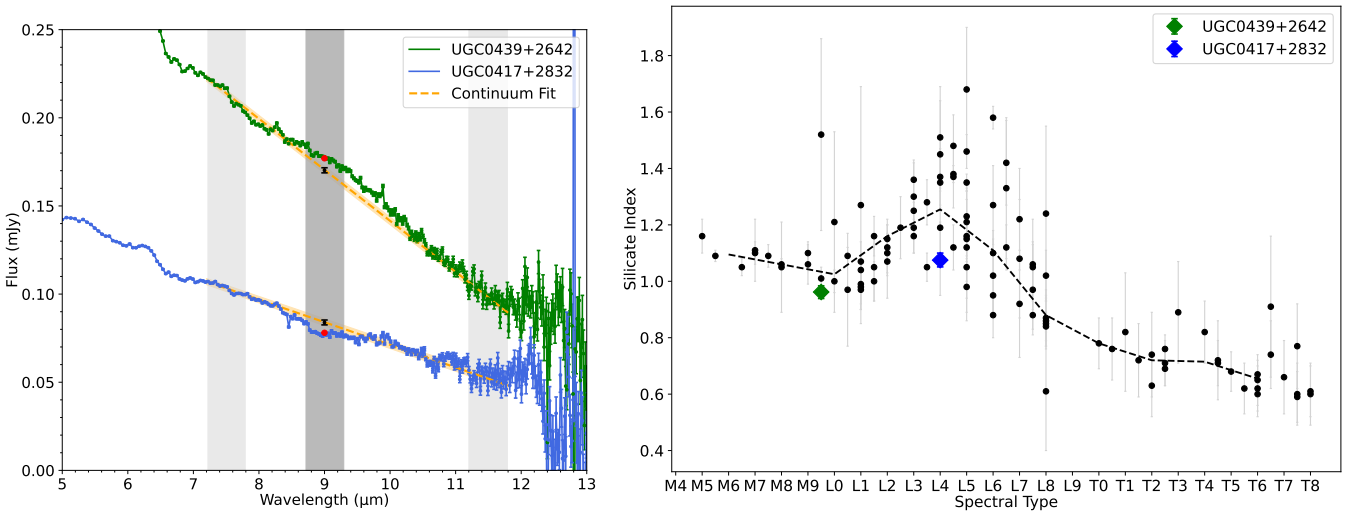

Figure 11. Left: measurement of silicate index for the two targets in our sample that do not show excess emission above the photosphere in the mid-infrared. Both the spectra are corrected for extinction using the K. D. Gordon et al. (2023) relation and A_V from Table 1. The vertical shaded regions of width 0.6 μm highlight the wavelength ranges used to fit the continuum (light gray) and the silicate absorption (dark gray). The orange dashed line and shaded region show the best linear fit to the continuum and the uncertainty, respectively. The black and red points mark the average flux at 9.0 μm. Right: silicate index as a function of spectral type for our two FFPMOs along with the index for dwarfs from G. Suárez & S. Metchev (2022). The error bars for the two FFPMOs indicate the range in silicate index when A_V changes by $\pm$1 mag. The black dashed curve is the median silicate index for bins of two spectral subtypes.

and 1900 K. We compare the near-infrared spectra with two dwarfs of similar spectral type, TWA 28 and VHS 1256 b, and find significant water absorption features in all our targets. We also see prominent CO_2 molecular absorption features in five of our targets, possibly attributable to high metallicity. We note that our targets show diversity in their spectra, especially in the 3–5 μm range, that is not well represented by photospheric models, pointing toward differences in cloud distribution and chemistry as plausible causes.

3. Six out of our eight targets exhibit mid-infrared excess emission above the photosphere, indicating the presence of disks around them. All of them show 10 μm silicate emission features from warm dust in the inner disk. These are the lowest-mass objects detected so far with such a feature arising in the disk. We measure the shape and strength of the silicate feature and find it to vary among our targets owing to the differences in grain growth and the degree of crystallization. Analogous to brown dwarfs, most of these FFPMOs show evidence for dust processing and crystallization, demonstrating the potential for the formation of rocky companions in the disks around free-floating planetary-mass objects.
4. Additionally, we report the detection of silicate absorption around 10 μm in one of our targets without a disk. This is the first time silicate absorption arising from clouds in the atmosphere has been found in a young FFPMO.
5. We also see molecular emission lines of methane and/or ethylene in a majority of our targets. These features are strongest in CHA1107-7626, as reported by L. Flagg et al. (2025). Characterization of the molecular emission in these sources requires higher-resolution observations.

Acknowledgments

The authors thank the anonymous referee for a constructive report that helped to improve the paper. We also would like to thank Ilaria Pascucci for helpful comments regarding the parameters plotted in Figure 10. B.D. and A.S. acknowledge support from the UKRI Science and Technology Facilities Council through grant ST/Y001419/1/. R.J. and L.F. acknowledge support for the JWST-GO-04583.008 program provided by NASA through a grant from the Space Telescope Science Institute, which is operated by the Association of Universities for Research in Astronomy, Inc., under NASA contract NAS 5–03127. V.A.-A. acknowledges support from the INAF grant 1.05.12.05.03. K.M. acknowledges support from the Fundação para a Ciência e a Tecnologia (FCT) through the grant 2022.03809.CEECIND, and the Scientific Visitor Programme of the European Southern Observatory (ESO) in Chile. P.P. acknowledges funding from the UK Research and Innovation (UKRI) under the UK government's Horizon Europe funding guarantee from ERC (under grant agreement No 101076489).

Facility: JWST.

Software: astropy (Astropy Collaboration et al. 2013, 2018).

ORCID iDs

Belinda Damian https://orcid.org/0000-0002-2234-4678
Aleks Scholz https://orcid.org/0000-0001-8993-5053
Ray Jayawardhana https://orcid.org/0000-0001-5349-6853
V. Almendros-Abad https://orcid.org/0000-0002-4945-9483
Laura Flagg https://orcid.org/0000-0001-6362-0571
Koraljka Mužić https://orcid.org/0000-0002-7989-2595
Antonella Natta https://orcid.org/0000-0002-4608-7995
Paola Pinilla https://orcid.org/0000-0001-8764-1780
Leonardo Testi https://orcid.org/0000-0003-1859-3070

References

Allard, F., Homeier, D., & Freytag, B. 2012, RSPTA, 370, 2765
Allers, K. N., & Liu, M. C. 2013, ApJ, 772, 79
Allers, K. N., & Liu, M. C. 2020, PASP, 132, 104401
Almendros-Abad, V., Mužić, K., Moitinho, A., Krone-Martins, A., & Kubiak, K. 2022, A&A, 657, A129

Apai, D., Pascucci, I., Bouwman, J., et al. 2005, Sci, 310, 834
Arabhavi, A. M., Kamp, I., Henning, T., et al. 2024, Sci, 384, 1086
Arabhavi, A. M., Kamp, I., Henning, T., et al. 2025, A&A, 699, A194
Astropy Collaboration, Price-Whelan, A. M., Sičcz, B. M., et al. 2018, AJ, 156, 123
Astropy Collaboration, Robitaille, T. P., Tollerud, E. J., et al. 2013, A&A, 558, A33
Bailer-Jones, C. A. L., Rybizki, J., Fouesneau, M., Demleitner, M., & Andrae, R. 2021, AJ, 161, 147
Baraffe, I., Homeier, D., Allard, F., & Chabrier, G. 2015, A&A, 577, A42
Bayo, A., Joergens, V., Liu, Y., et al. 2017, ApJL, 841, L11
Boersma, C., Allamandola, L. J., Esposito, V. J., et al. 2023, ApJ, 959, 74
Burgasser, A. J. 2014, arXiv:1406.4887
Bushouse, H., Eisenhamer, J., Dencheva, N., et al. 2024, JWST Calibration Pipeline, v1.15.1, Zenodo, doi:10.5281/zenodo.12692459
Cieza, L., Padgett, D. L., Stapelfeldt, K. R., et al. 2007, ApJ, 667, 308
Cruz, K. L., Núñez, A., Burgasser, A. J., et al. 2018, AJ, 155, 34
Cushing, M. C., Roellig, T. L., Marley, M. S., et al. 2006, ApJ, 648, 614
Damian, B., Jose, J., Biller, B., & Paul, K. T. 2023a, JApA, 44, 77
Damian, B., Jose, J., Biller, B., et al. 2023b, ApJ, 951, 139
Decleir, M., Gordon, K. D., Andrews, J. E., et al. 2022, ApJ, 930, 15
Delorme, P., Gagné, J., Malo, L., et al. 2012, A&A, 548, A26
Dupuy, T. J., Liu, M. C., Evans, E. L., et al. 2023, MNRAS, 519, 1688
Dupuy, T. J., Liu, M. C., Magnier, E. A., et al. 2020, RNAAS, 4, 54
Esplin, T. L., & Luhman, K. L. 2019, AJ, 158, 54
Esplin, T. L., & Luhman, K. L. 2020, AJ, 159, 282
Esplin, T. L., Luhman, K. L., Faherty, J. K., Mamajek, E. E., & Bochanski, J. J. 2017, AJ, 154, 46
Fitzpatrick, E. L. 1999, PASP, 111, 63
Flagg, L., Scholz, A., Almendros-Abad, V., et al. 2025, ApJ, 986, 200
Franceschi, R., Henning, T., Tabone, B., et al. 2024, A&A, 687, A96
Gagné, J., Faherty, J. K., Cruz, K. L., et al. 2015, ApJS, 219, 33
Gaia Collaboration, Prusti, T., de Bruijne, J. H. J., et al. 2016, A&A, 595, A1
Gaia Collaboration, Vallenari, A., Brown, A. G. A., et al. 2023, A&A, 674, A1
Gordon, K. D., Cartledge, S., & Clayton, G. C. 2009, ApJ, 705, 1320
Gordon, K. D., Clayton, G. C., Decleir, M., et al. 2023, ApJ, 950, 86
Gordon, K. D., Misselt, K. A., Bouwman, J., et al. 2021, ApJ, 916, 33
Hurt, S. A., Liu, M. C., Zhang, Z., et al. 2024, ApJ, 961, 121
Jayawardhana, R., Ardila, D. R., Stelzer, B., & Haisch, K. E., Jr. 2003, AJ, 126, 1515
Jayawardhana, R., & Ivanov, V. D. 2006, Sci, 313, 1279
Joergens, V., Bonnefoy, M., Liu, Y., et al. 2013, A&A, 558, L7
JWST Transiting Exoplanet Community Early Release Science Team, Ahrer, E.-M., Alderson, L., et al. 2023, Natur, 614, 649
Langeveld, A. B., Scholz, A., Mužić, K., et al. 2024, AJ, 168, 179
Lucas, P. W., & Roche, P. F. 2000, MNRAS, 314, 858
Luhman, K. L. 2007, ApJS, 173, 104
Luhman, K. L., Adame, L., D'Alessio, P., et al. 2005, ApJL, 635, L93
Luhman, K. L., Allen, L. E., Allen, P. R., et al. 2008, ApJ, 675, 1375
Luhman, K. L., & Alves de Oliveira, C. 2025, ApJL, 986, L14
Luhman, K. L., Mamajek, E. E., Shukla, S. J., & Loutrel, N. P. 2017, AJ, 153, 46
Manjavacas, E., Tremblin, P., Birkmann, S., et al. 2024, AJ, 167, 168
Martín, E. L., Žerjal, M., Bouy, H., et al. 2025, A&A, 697, A7
Miles, B. E., Biller, B. A., Patapis, P., et al. 2023, ApJL, 946, L6
Miret-Roig, N., Bouy, H., Raymond, S. N., et al. 2022, NatAs, 6, 89
Mohanty, S., Jayawardhana, R., Natta, A., et al. 2004, ApJL, 609, L33
Mužić, K., Scholz, A., Geers, V. C., Jayawardhana, R., & López Martí, B. 2014, ApJ, 785, 159
Natta, A., & Testi, L. 2001, A&A, 376, L22
Pascucci, I., Apai, D., Luhman, K., et al. 2009, ApJ, 696, 143
Phillips, M. W., Tremblin, P., Baraffe, I., et al. 2020, A&A, 637, A38
Pinilla, P. 2022, EPJP, 137, 1206
Piscarreta, L., Mužić, K., Almendros-Abad, V., & Scholz, A. 2024, A&A, 686, A37
Radigan, J., Lafrenière, D., Jayawardhana, R., & Artigau, E. 2014, ApJ, 793, 75
Rigby, J., Perrin, M., McElwain, M., et al. 2023, PASP, 135, 048001
Sanghi, A., Liu, M. C., Best, W. M. J., et al. 2023, ApJ, 959, 63
Schneider, A. C., Windsor, J., Cushing, M. C., Kirkpatrick, J. D., & Wright, E. L. 2016, ApJL, 822, L1
Scholz, A., & Jayawardhana, R. 2008, ApJL, 672, L49
Scholz, A., Jayawardhana, R., Muzic, K., et al. 2012, ApJ, 756, 24
Scholz, A., Jayawardhana, R., Wood, K., et al. 2007, ApJ, 660, 1517
Scholz, A., Muzic, K., Jayawardhana, R., Almendros-Abad, V., & Wilson, I. 2023, AJ, 165, 196
Scholz, R. D., McCaughrean, M. J., Zinnecker, H., & Lodieu, N. 2005, A&A, 430, L49
Seo, H. H., & Scholz, A. 2025, MNRAS, 537, 2579
Sorahana, S., & Yamamura, I. 2012, ApJ, 760, 151
Suárez, G., & Metchev, S. 2022, MNRAS, 513, 5701
Suárez, G., Vos, J. M., Metchev, S., Faherty, J. K., & Cruz, K. 2023, ApJL, 954, L6
Teixeira, P. S., Lada, C. J., Marengo, M., & Lada, E. A. 2012, A&A, 540, A83
Tsuji, T., Yamamura, I., & Sorahana, S. 2011, ApJ, 734, 73
Venuti, L., Stelzer, B., Alcalá, J. M., et al. 2019, A&A, 632, A46
Vos, J. M., Allers, K. N., & Biller, B. A. 2017, ApJ, 842, 78
Zapatero Osorio, M. R., Béjar, V. J. S., Martín, E. L., et al. 2000, Sci, 290, 103